# Optical frequency reference based on a cryogenic silicon resonator

Eugen Wiens, Chang Jian Kwong, Timo Müller, Kai Bongs, Yeshpal Singh, Stephan Schiller

Article - Version of Record

Suggested Citation:
Wiens, E., Kwong, C. J., Müller, T., Bongs, K., Singh, Y., & Schiller, S. (2023). Optical frequency reference based on a cryogenic silicon resonator. Optics Express, 31(25), 42059–42076.
https://doi.org/10.1364/oe.497365

Research Article | Vol. 31, No. 25 / 4 Dec 2023 / Optics Express 42059

Optics EXPRESS

# Optical frequency reference based on a cryogenic silicon resonator

EUGEN WIENS,[1,*] CHANG JIAN KWONG,[1] TIMO MÜLLER,[2] KAI BONGS,[3,4] YESHPAL SINGH,[3] AND STEPHAN SCHILLER[1]

[1] *Institut für Experimentalphysik, Heinrich-Heine-Universität, Düsseldorf, 40225 Düsseldorf, Germany*
[2] *Siltronic AG, Johannes-Hess-Straße 24, 84489 Burghausen, Germany*
[3] *School of Physics and Astronomy, University of Birmingham, Birmingham B15 2TT, UK*
[4] *Now at the German Aerospace Center (DLR), Institute of Quantum Technologies, 89081 Ulm, Germany*
[*] *eugen.wiens@hhu.de*

**Abstract:** We present the development and in-depth characterization of an optical reference based on a 1.5 $\mu$m laser stabilized to a cryogenic silicon optical resonator operated at 1.7 K. The closed-cycle cryostat is equipped with a cryogenic passive vibration isolation. At $\tau = 1$ s integration time the frequency instability is $2 \times 10^{-14}$, predominantly due to residual vibrations. At $\tau = 100$ s the frequency instability is $6.2 \times 10^{-15}$. The lowest instability of $3.5 \times 10^{-16}$ occurs at $\tau = 6000$ s, and is limited by the stability of the hydrogen maser used in the comparison. The mean fractional frequency drift rate over 190 days was $-3.7 \times 10^{-20}$/s. In conjunction with a frequency comb and a GNSS receiver this optical reference would be suitable to provide optical frequencies with accuracies at the low $10^{-14}$ level. We show that residual vibrations affect the resonator and the optical fiber delivering the laser light to it, and that laboratory temperature variations contribute to frequency instability at short and medium integration times. Mitigation of these issues might in the future allow for demonstration of the thermal-noise-limited performance of the resonator.



## 1. Introduction

The precision of a range of laser-based experiments is determined by the frequency stability and spectral purity of the employed laser wave. Optical resonators represent to date the most common tool for the stabilization of laser frequency. Moreover, resonators also serve as the sensing unit of certain instruments. Thus, resonators are routinely used in different fields, e.g., laser spectroscopy [1], gravitational-wave detectors [2–4], optical atomic clocks [1,5], dark-matter detection [6–9], very-long-baseline interferometry [10], astronomy [11,12], relativistic geodesy [13–15] and tests of fundamental physics [16–19].

To achieve extreme frequency stability of the laser wave requires isolating the reference resonator from all kinds of environmental perturbations that influence its length significantly, such as vibrations, tilt, temperature and pressure variations, thermo-elastic deformations of mirrors due to the fluctuating laser power, and material creep. This is usually done using passive and/or active isolation/stabilization techniques together with a careful choice of resonator material, for which a low sensitivity to the variations of the parameter in question is sought. In addition to this, the shape of the resonator and the support structure are optimized in order to reduce the vibration sensitivity of the resonator.

Ultra-low-expansion glass (ULE) and, less commonly, Nexcera ceramics [20–23] are the materials of choice for construction of room-temperature resonators. However, because they are operated at room temperature, they exhibit a relatively high thermal noise limit [24] and

#497365 https://doi.org/10.1364/OE.497365
Journal © 2023 Received 7 Jun 2023; revised 23 Oct 2023; accepted 29 Oct 2023; published 29 Nov 2023

furthermore a continuous change of length due to aging (creep). To reduce these limitations, cryogenic operation of resonators made of suitable materials provides a solution [18,25–33].

In this work, we present an apparatus that aims to be a reliable *optical* frequency reference for frequency metrology experiments. One aimed-for feature is an excellent long-term stability, which would be very helpful in facilitating experimentation where ultra-narrow atomic or molecular resonances are interrogated repeatedly over a long time. With that feature, the optical reference would be a viable alternative to an ultrastable radiofrequency reference, such as an active hydrogen maser, plus a femtosecond frequency comb that generates optical frequencies from the radiofrequency.

Our realization of the optical reference is a cryogenic single-crystal silicon resonator operated inside a closed-cycle cryostat at 1.7 K. The resonator is the reference to which a fiber laser's frequency is stabilized. The cryostat is based on a pulse-tube cooler combined with a Joule-Thomson stage able to reach 1.5 K. A unique feature of our cryostat is that the plate supporting the experimental payload inside the cryostat is shielded from vibrations using a passive vibration isolation. It was developed by some of the present authors and is described in Ref. [34].

In previous work, we demonstrated the performance of a vertically oriented 5 cm resonator operated in the same cryostat, however without any vibration isolation [33]. This resonator had a relatively low finesse and correspondingly large linewidth, which made it difficult to achieve low frequency instability. Further progress in this direction required a resonator with longer spacer and high-finesse mirrors. Thus, we built a vertically-oriented, biconically-shaped resonator with a length of 190 mm. The overall design of this resonator resembles that of a 212 mm silicon resonator developed and operated by PTB [30]. However, with exception of a diameter and thickness of the middle ring, all dimensions are different. In the following we present results of the characterization of the resonator obtained with the help of a stable interrogation laser, two frequency combs, and two hydrogen masers.

## 2. Resonator design

The vertically oriented resonator has a biconical, axially symmetric geometry and is supported at three points. This design follows the concept presented in Refs. [27–31,33]. The overall size of the resonator is restricted by the length and diameter of the available silicon ingot material oriented along the [111] crystallographic direction. We fixed the spacer length to 190 mm, the largest outer diameter of the resonator to 78 mm, the outer diameter of the supporting ring to 96 mm, the thickness of the supporting ring to 10 mm. The diameter of the central bore was fixed to 10 mm. The diameter of the spacer at the ends of the biconical surfaces was set to 26 mm. The radial distance of the support points from the symmetry axis of the resonator was set to 42.9 mm. One of the supports is oriented along the radial line that coincides with the [100] crystallographic direction of the silicon crystal. Three venting holes of 3 mm diameter are located in the upper half of the resonator. They are positioned exactly above the three supports (spaced by 120 degrees) and at a distance of 82 mm below the top surface. We employed silicon mirror substrates with a standard one-inch diameter and a thickness of 6.3 mm. After optical contacting to the spacer, they form a single body with the spacer. We apply the silicon stiffness matrix from Ref. [35] in our simulation.

The above choices left the offset of the middle ring from the horizontal midplane to be optimized. We varied this parameter and for each choice performed finite-element-method (FEM) determination of the effect of gravity. We used the Ansys modeling software package [36]. Specifically, in the calculation we applied an acceleration equal to the free-fall acceleration $g$ to the whole body of the resonator and calculated the resulting change of distance, $\Delta L$, between the centers of the two mirrors. We searched for a position of the support ring that minimized $\Delta L$. The optimization result is depicted in Fig. 1(a). It shows the deformation of the resonator under the influence of a vertical acceleration $g$ applied to all volume elements. The resonator is here supported at three points under the middle ring. The simulation finds that both mirror centers are vertically shifted down by the same value of 22 nm, leaving the distance between them and thus the optical path length for the resonating wave unchanged, $\Delta L = 0$. Note that 22 nm is approximately $1 \times 10^{-7}$ relative to the mirror spacing, and one aims for a common mode rejection of this displacement on the order of 1 part in $10^4$, i.e. $\Delta L/L \simeq 1 \times 10^{-11}$. The goal vibration (acceleration) sensitivity is therefore $1 \times 10^{-11}/g$.

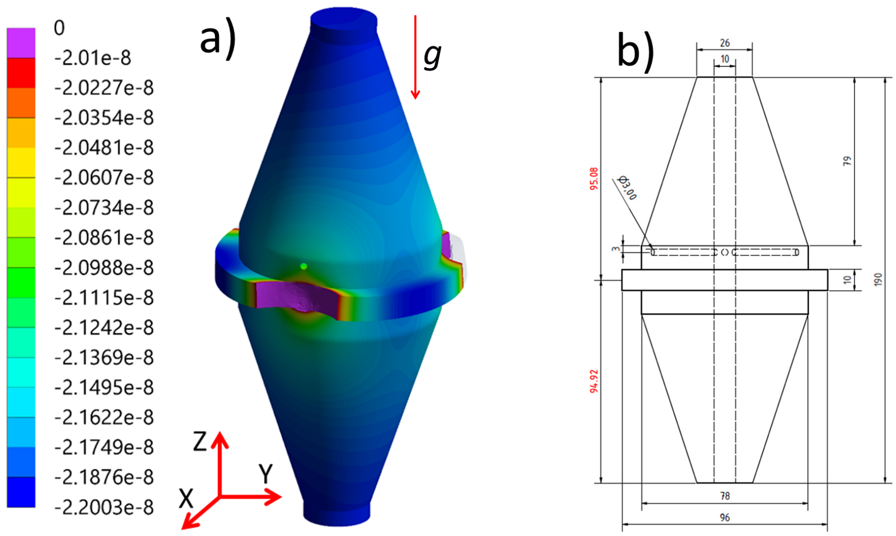


**Fig. 1.** a) FEM simulation of the effect of gravity on the resonator having optimized shape. Color indicates the displacement in meter along the vertical direction (z-axis) due to the application of 1 $g$ vertical acceleration. To increase the visibility of the displacement of the mirrors, parts of the support ring around the underlying supports were removed from the representation. b) Resonator design with the offset of the middle ring optimized relative to the horizontal midplane of the resonator using FEM simulations. The optimal offset is equivalently displayed here as the difference in the distance from the middle ring to the end faces of the resonator (dimensions highlighted in red). Distances are in mm.

The optimized shape of the resonator is presented in Fig. 1(b). It is symmetrical, with an offset of the ring from the horizontal symmetry plane by 0.1 mm in the direction of the top surface.

We also simulated the influence of possible errors in the manufacturing of the spacer, errors in the alignment of the mirror substrates relative to the optical axis, and errors in the orientation of the resonator relative to the supports points. These errors have a negative effect on the vibration sensitivity of the resonator. For the above support setting, the acceleration sensitivity induced by a typical error of 0.1 mm in the manufacturing of the support ring offset is $5.7 \times 10^{-12}/g$. The sensitivity to a misalignment of the support radial position is $2.1 \times 10^{-11}/(g \cdot \mathrm{mm})$, the sensitivity to a single mirror radial misalignment relative to the symmetry axis of the resonator is $4 \times 10^{-11}/(g \cdot \mathrm{mm})$, and the sensitivity to axial rotation of the resonator relative to the support points is $5 \times 10^{-12}/(g \cdot \mathrm{deg})$. For typical expected errors of 0.1 - 1 mm and 5 deg, the resulting theoretical sensitivities would remain small.

## 3. Apparatus

### *3.1. Resonator and resonator support*

The resonator is manufactured from a 4-inch-diameter cylindrical silicon crystal, grown along the [111] crystallographic direction using the float zone method [37]. Its resitivity is 8 kOhm/cm. The two end faces of the resonator were polished to optical quality. Two high-reflectivity dielectric silicon mirrors for 1.5 $\mu$m wavelength were optically contacted to them. Because of availability, these silicon substrates are manufactured from a different block of material oriented along the [100] crystallographic direction and having a resistivity of 4 kOhm/cm. This aspect was not considered in the above simulations.

The resonator and the corresponding optical setup are installed inside a pulse-tube cryostat equipped with a Joule-Thomson stage (Leiden Cryogenics) and a home-built passive vibration isolation [34]. A picture of the setup is presented in Fig. 2. The resonator is supported at three points by pressure screws having stainless steel balls at their ends. The upper part of the balls is removed to produce a circular surface of 3 mm diameter. The temperature of resonator is measured with a sensor (Cernox) attached to the top surface of the support ring using a cryogenic grease. To low-pass filter the fluctuations of cryostat temperature, the support structure is manufactured from a stainless steel (SS304). The latter dampens the thermal flow, given its reduced thermal conductivity compared to silicon, copper and aluminum.


**Fig. 2.** The silicon cavity supported by a stainless-steel support structure. A few numbered components are 1) flat mirror of resonator; 2) resonator temperature sensor; 3) stainless-steel support ring attached to a tripod; 4) concave mirror of resonator.

Optics EXPRESS

### 3.2. Cryogenic optical setup

The coupling of the laser light into the resonator is implemented using a compact optical setup installed on the bottom surface of the experimentation plate, see Fig. 3. The light of the laser is guided to the setup via a single-mode polarization-maintaining fiber. A standard fiber collimator is attached to the end of the fiber. A partially reflective mirror is installed next to the collimator. The back-reflected light is used for the characterization of fiber-noise-induced spectral broadening of the laser light (see Sec. 4.1). After transmission through the partially reflective mirror, the laser wave is coupled into the resonator with the help of two adjustable mirrors and a 90 degree fixed mirror. The total optical path length between fiber collimator and the resonator is minimized in order to reduce the effect of unavoidable misalignments upon cooling down to cryogenic temperature. To allow for readjustment of the laser beam into the resonator after the cooldown we equipped the two adjustable mirror mounts with commercial stepper motors, that are adapted in-house for cryogenic operation. At the top surface of the experimentation plate and below the resonator a polarizing beam splitter and a quarter-wave plate are installed (not shown). After partial reflection at the bottom mirror of the resonator the light is detected by a high-bandwidth photodetector (not shown). The position of this detector can be optimized with the help of a x-z cryogenic motorized translation stage. The light transmitted through the resonator and exiting on the top is split by a beam splitter. One part is detected by a photodiode. The other part is used for mode identification with a room-temperature InGaAs camera during the installation phase, while the cryostat is open. Due to the shrinkage of the elements of the passive vibration isolation by about 1.5 cm during the cooldown, once base temperature is reached the laser light cannot exit the cryostat any more. This prevents mode identification after the cooldown.

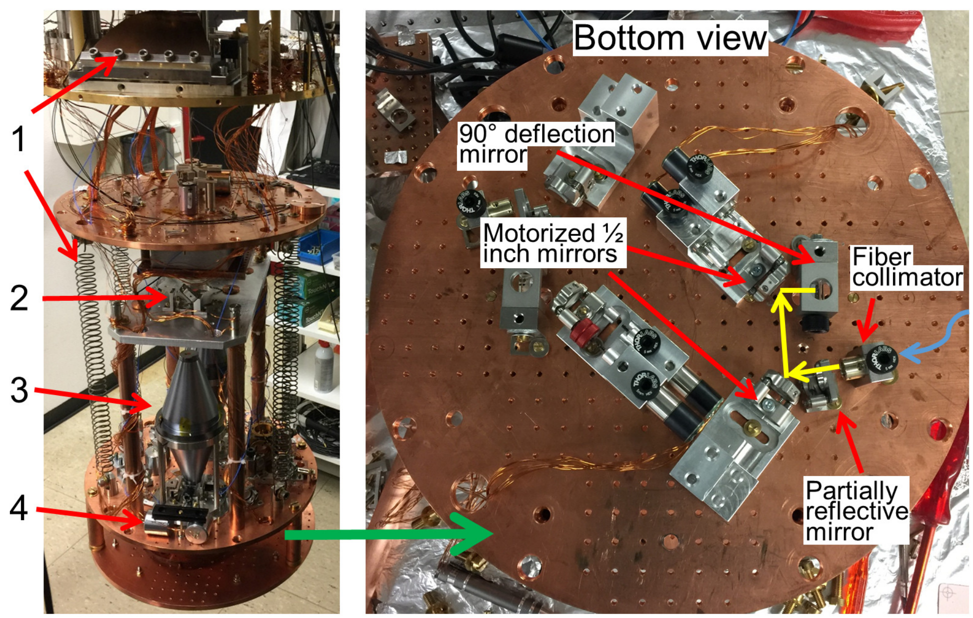


**Fig. 3.** Left: overall view of the resonator inside the opened cryostat. The following units are indicated: 1) passive vibration isolation; 2) transmission photodiode; 3) silicon resonator with support; 4) geophones. Right: The bottom of the experimentation plate with the optical setup. Yellow arrows indicate the path of the free-space laser beam. The blue-colored arrow indicates where the optical fiber will be attached.

Optics EXPRESS

### 3.3. Optical frequency stabilization system

The purpose of the cryogenic system is to substantially improve the medium ($\tau$>20 s) and long-time ($\tau$>1000 s) stability of a laser already having a good short-term frequency stability. The concept of the laser and resonator interrogation technique is identical to our previous work presented in [33]. The fiber laser is pre-stabilized to a 10 cm long ULE room-temperature reference resonator. Its frequency is subsequently stabilized to the cryogenic resonator. The schematic of the optical setup is presented in Fig. 4.

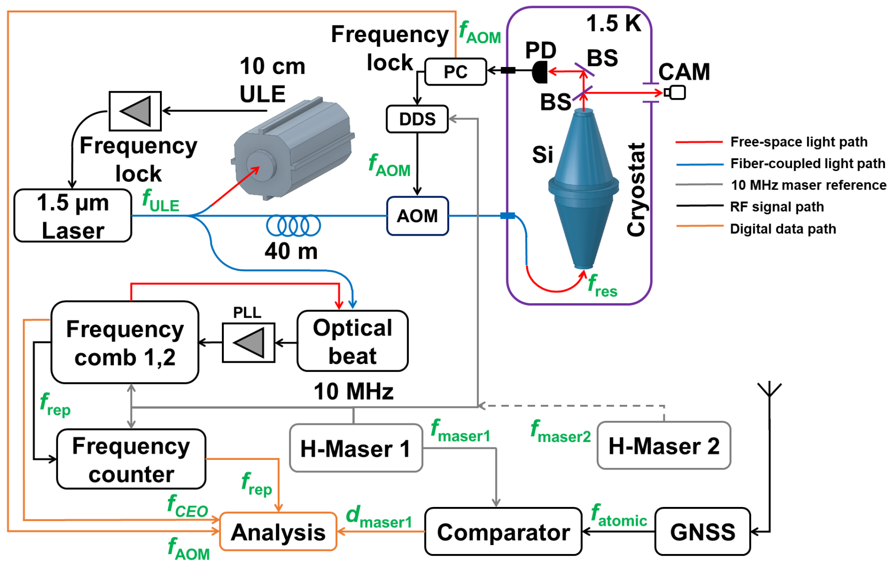


**Fig. 4.** Overall experimental setup. Red and blue lines indicate free-space and fiber-coupled paths, respectively. Black lines represent the electronic paths and the gray line is the 10 MHz reference signal from the hydrogen maser. $f_{\mathrm{res}}$, frequency of the cryogenic silicon resonator; $f_{\mathrm{ULE}}$, frequency of the room-temperature ULE resonator; $f_{\mathrm{atomic}}$, frequency of the GNSS satellite signal; $f_{\mathrm{maser1}}$ and $f_{\mathrm{maser2}}$, frequencies of two hydrogen masers; $d_{maser1}$, frequency drift of the hydrogen maser 1; $f_{\mathrm{rep}}$, repetition rate of the frequency comb one or two; $f_{\mathrm{CEO}}$, carrier envelope offset of the frequency comb one or two; $f_{\mathrm{AOM}}$, frequency of the AOM; PC, personal computer; AOM, acousto-optical modulator; DDS, direct digital synthesizer; PD, photodiode; BS, beam splitter; CAM, InGaAs infrared camera for mode detection.

A part of a pre-stabilized laser light (optical frequency $f_{\mathrm{ULE}}$) having a linewidth of approximately 1 Hz is transferred up to the cryostat in the cryogenic lab via a 40 m long optical fiber. Active fiber noise cancellation is not implemented. This results in a time-dependent broadening of the linewidth to approximately 30 Hz due to the fiber noise along this path. An additional 10 m long fiber with a vacuum fiber feedthrough guides the laser light all the way to the cryogenic optical setup of the silicon resonator. The length of the fiber inside the cryostat downstream the vacuum feedthrough is 3 m and along this path substantial further frequency noise is introduced, caused by the vibrations of the cooler (see next section).

We steer the frequency of the laser to a chosen mode of the cryogenic silicon resonator by means of an acousto-optic frequency shifter (AOM, frequency $f_{\mathrm{AOM}}$). We continuously determine the mode's center frequency using a fringe interrogation technique. For this, we alternately measure the light levels $A_{\mathrm{L}}$, $A_{\mathrm{R}}$ transmitted through the resonator when the laser frequency is detuned by $\delta f_{\mathrm{AOM}} \simeq -\Delta\nu/2$ and $+\Delta\nu/2$ from resonance, where $\Delta\nu$ is the full width at half maximum of the fringe (cavity resonance line). The detuning is produced by acting on the AOM frequency. After both signals have been recorded by a data acquisition system, a frequency correction is calculated, $\Delta f_{\mathrm{AOM}} = (\Delta\nu/2)(A_L - A_R)/(A_L + A_R)$. This correction, effectively rounded to integer values in Hz by the finite resolution of the DDS, is applied to the AOM frequency $f_{\mathrm{AOM}}$ and the whole measurement cycle is repeated. As a result, the laser wave frequency-shifted by the AOM has a time-averaged frequency equal to the resonator frequency.

$A_{\mathrm{L}}$ and $A_{\mathrm{R}}$ are measured by a DAQ card with a sampling rate of 40 kS/s and 16 bit resolution. The integration time of each measurement $A_{\mathrm{L}}$, $A_{\mathrm{R}}$ is initially set to 250 ms. In the later course of the experimentation this time was reduced to 150 ms. The AOM is driven by a home-built direct digital synthesizer (DDS) with a 1 Hz frequency resolution. The DDS is referenced to the maser and controlled by a personal computer (PC), where the stabilization is digitally implemented.

To determine the impact of the finite resolution of the DDS on the lock, a simple numerical simulation of the lock was made. To account for the relative fluctuation of the interrogation laser to the transmission mode of the resonator, a random fluctuation of the frequency of the interrogation laser in the [-15, 15] Hz range was introduced in each measurement cycle. A linear frequency drift of the interrogation laser equal to 0.1 Hz/s was also included into the simulation. The finite resolution of the DDS was taken into account by rounding the correction frequency of the AOM $f_{\mathrm{AOM}}$ (in units Hz) to the nearest integer after each iteration. The simulation reveals that the uncertainty in the offset between interrogation laser and resonator scales down like $0.29\sqrt{0.15/\tau}$ Hz, where $\tau$ is the integration time in s. The uncertainty can be neglected for $\tau \geq 1$ s. The 16 bit resolution of the DAQ card is another source of uncertainty. It introduces a quantization noise equal to 0.15 mV during each measurement cycle, which corresponds to 0.3 Hz frequency uncertainty and scales down to 0.12 Hz and less for $\tau \geq 1$ s and therefore can be neglected.

The laser frequency $f_{\mathrm{ULE}}$ is measured relative to the frequency $f_{\mathrm{maser1}}$ of an active hydrogen maser (H-maser) with a frequency comb. To increase the precision of the laser frequency measurements we phase-lock the comb's repetition rate to the prestabilized laser frequency. Thus, the absolute optical frequency of the resonator, $f_{\mathrm{res}}$, can be calculated as the sum of $f_{\mathrm{ULE}}$ and $f_{\mathrm{AOM}}$, both available in numerical form.

The maser frequency $f_{\mathrm{maser1}}$ is continuously measured relative to a GNSS time signal that represents an atomic reference $f_{\mathrm{atomic}}$. By analyzing this data, we can determine the maser's frequency drift rate $d_{\mathrm{maser1}}$. Correcting for it, we thus are able to determine the resonator frequency (and mean laser wave frequency) relative to the atomic reference frequency delivered by GNSS.

In the course of this work two frequency combs FC1 and FC2 (both Menlo Systems) were used. We initially used an active hydrogen maser 1 (Vremya-ch), that was later replaced with another, recently produced T4Science maser [38] having better stability (H-Maser 2 in Fig. 4). The maser was operated inside the heat control box (HCB) during the presented measurements.

## 4. Characterization of the system

### 4.1. Noise in the cryogenic optical fiber

Vibrations of the cryostat induce mechanical stress in the fiber that is installed inside the cryostat to transport the laser light to the resonator. This noise is measured using the optical setup described in Ref. [39]. A beat between the incoming laser light and the light back-reflected at the mirror installed at the cryogenic end of the fiber is generated outside the cryostat. The spectrum of the beat is displayed in panel a of Fig. 5. A comparison with the spectrum taken when the pulse-tube cooler is briefly turned off indicates substantial broadening by cooler-induced vibrations. The broadening of the laser carrier component after a single pass through the fiber is approximately 16 Hz with side peaks at frequencies approximately equal to 7 Hz and 14 Hz. These are 5× and 10× multiples of 1.4 Hz, the pulsing rate of the high-pressure helium gas inside the pulse tube of the cryostat (see panel b in Fig. 5). Additional sidebands occur at multiples of 141 Hz, the frequency of the stepper motor that drives the rotary valve of the pulse-tube cooler.

This spectral broadening has a significant impact on the short-term frequency stability of the laser, on time scales of less than 1 s integration.

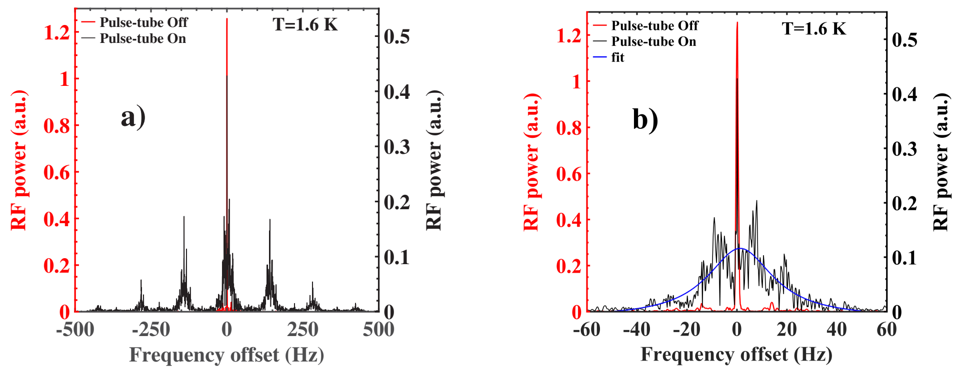


**Fig. 5.** a) Laser line broadening after double passage through the cryogenic fiber. The self-beat is shown. b) Zoom into the central peak with the Lorentzian fit of the broadened self-beat. The scale of both vertical axis is identical to those in a.

It was not possible to implement a fiber noise cancellation system during the measurement campaign, because during regular operation it was not possible to reflect sufficient optical power back into the fiber from the cryogenic mirror. The reason was the small coupling efficiency of the light back-reflected from the partially reflective mirror into the cryogenic end of the fiber. This could not be compensated by injecting more power into the fiber because this would have led to too much power impinging on the cavity.

### 4.2. Optimization of resonator coupling

During the cooldown a degradation of the incoupling was observed. Thus, at 4 K a readjustment of the cryogenic laser path was required. As described in Sec. 3.2, in steady-state operation, the wave transmitted through the resonator did not reach the camera any more, preventing direct identification of the cavity mode type. In order to proceed, we first scanned over all modes within one spectral free range of the resonator, 789 MHz. We covered this range by frequency shifting the prestabilized laser light using different AOMs and combinations of AOMs. After all modes were found, we then identified the mode with the smallest linewidth. It occured at a convenient AOM frequency $f_{\text{AOM}} \simeq 40$ MHz. The coupling into this mode was then optimized by adjusting the motorized mirror mounts. We obtained an incoupling of 7% and a mode matching efficiency of 70%. The linewidth of this mode was 4 kHz, corresponding to a finesse of 200 000. In Fig. 6 a scan of this mode is presented. The influence of the cryostat vibrations on the transmission signal is clearly present in the data. The periodic disturbances are due to periodic variations of the input wave's coupling into the resonator caused by modulation of resonator length due to vibrations. In other words, vibration-induced cavity detuning leads to incoupling variations. This effect allows for determination of resonator sensitivity to vibrations, presented in the next section.

### 4.3. Acceleration sensitivity

The sensitivity of resonator mirror spacing to acceleration is determined using the transmission photodiode signal when the laser frequency is tuned to the half-maximum of the resonance line (see Fig. 7(a)). We convert the units of the photodiode signal to Hz by applying the conversion factor $S = 0.48$ a.u./kHz, given by the slope of the transmission signal at the half-maximum value (see Fig. 6). The resulting time trace, depicted in Fig. 7(a), represents the variation of the resonance frequency of the silicon resonator relative to the frequency of the stabilized laser.

Optics EXPRESS

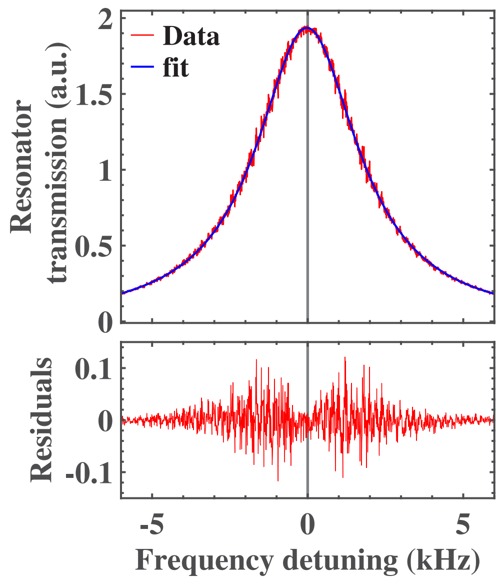


**Fig. 6.** One-way frequency scan of the pre-stabilized laser frequency over the resonator mode. Scan duration is 60 s. The signal is the light power transmitted through the resonator. The pulse-tube cooler is on. The blue line is a Lorentzian fit. Operating temperature: 1.6 K.

We observe a modulation at 4.2 Hz, the third harmonic of the pulse-tube frequency. The peak amplitude of the frequency modulation is slightly less than 200 Hz. The root-mean-square frequency variation $\delta f_{\mathrm{res}}$ of the resonator relative to the laser is 66 Hz. We interpret this as the vibration-induced broadening that would occur if a laser were tightly locked to the resonance.

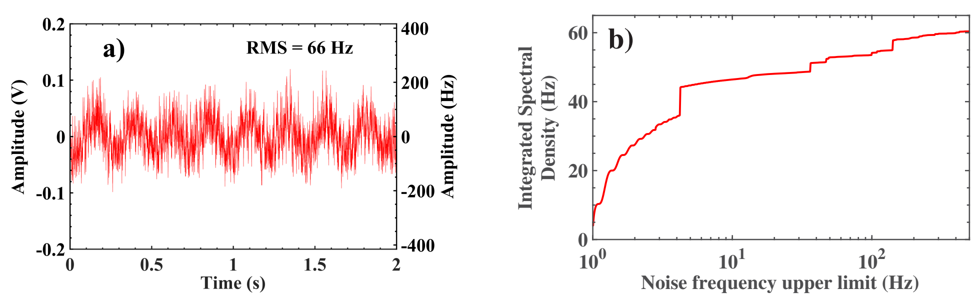


**Fig. 7.** Determination of the resonator sensitivity to vibrations. a) Time trace of the resonator transmission signal, with subtracted offset, measured with the laser frequency tuned to the half-transmission of the resonance line. Note that the light power used in this measurement differs from that in Fig. 6(b). Integrated power spectrum of the frequency fluctuations in a), as a function of upper limit of integration.

To obtain the frequency dependent contributions to the broadening of the resonance frequency we first compute the spectral density of frequency fluctuations from the time trace in Fig. 7(a). Then we compute the square root of the integral of the spectral density over the frequency range from 1 Hz up to frequency upper limit. The RMS value is plotted for various upper frequency limits in panel b of Fig. 7, and gives evidence that the largest contribution comes from the low-frequency band at and below 5 Hz. This can be explained by the fact that the passive vibration isolation does not attenuate sufficiently in this band [34].

In the band above 5 Hz vibrations are effectively reduced by the isolation. Thus, we believe that the contribution of 16 Hz to the integrated spectral density in this frequency band arises mainly from fiber-induced noise.

To calculate the acceleration sensitivity we first correct $\delta f_{\mathrm{res}}$ for the 16 Hz linewidth broadening of the laser carrier component due to passage through the fiber. Thus, we obtain $\delta f_{\mathrm{res}} = 50$ Hz. The total acceleration (integrated between 1 and 200 Hz) has the level $a_{\mathrm{total}} = 7.3 \times 10^{-4}\ g$ [34]. The acceleration sensitivity may be defined as the ratio of these two quantities, $\delta f_{\mathrm{res}}/a_{\mathrm{total}}$, and is equal to 68 kHz/$g$ or $3.6 \times 10^{-10}/g$ in fractional terms. This sensitivity is substantially higher than the theoretical sensitivity computed from FEM neglecting shape or positioning errors. The observed sensitivity could be due to imprecise manual positioning of the resonator relative to the support screws. This probably results in the position of the resonator being shifted along one horizontal direction relative to support. An additional increase in the sensitivity is due to the support screws with 3 mm$^2$ area of contact compared to the supports with 1.2 mm$^2$ contact area used in FEM simulations.

In the future the positioning might be optimized in the cold state with the help of motors and translation stages. This would allow to move as well as to rotate the resonator around its optical axis, allowing for determination of the optimal position relative to the support points.

### 4.4. Coefficient of thermal sensitivity

We determined the coefficient of thermal sensitivity of resonator frequency (CTF), $\alpha_{\mathrm{res}}(T)$, in the temperature range $T$ between 1.58 K and 4 K as follows. We heated the experimental payload with a heater mounted on the experimentation plate during 3.5 hours. Subsequently, to accelerate heating, the Joule-Thomson stage was switched off and He gas was pumped out of it. After an additional 1.5 hours 4 K was reached. At that point, we switched off the heater and turned on the Joule-Thomson cooler again, cooling down to the start temperature within 3 h. As the payload heated up and cooled down, two temperatures and the resonator frequency variation were recorded. The latter was recorded using the line interrogation technique outlined above.

The data is presented in Fig. 8(a). The total change of the resonator frequency over the temperature range is approximately 4 kHz, which is only $2 \times 10^{-11}$ fractionally. This is comparable to the result of Ref. [32]. To extract the CTF we first relate the frequency change to the temperature, see Fig. 8(b). This data is fit with a polynomial function $f(T) = aT^6 + bT^5 + cT^4 + d$, that includes an expected $T^3$ dependence of the CTF. The fit is shown as a red line in Fig. 8(b). The CTF is obtained from the fit result as $\alpha_{\mathrm{res}}(T) = -f_{\mathrm{res}}^{-1} df(T)/dT$, where $f_{\mathrm{res}} = 191.975$ THz. The result is $\alpha_{\mathrm{res}}(1.58\,\mathrm{K} < T < 4.0\,\mathrm{K}) = (-5.3(T/\mathrm{K})^5 + 39.4\,(T/\mathrm{K})^4 - 37.5\,(T/\mathrm{K})^3) \times 10^{-14}\mathrm{K}^{-1}$. The fit uncertainties of the coefficients are approximately 2% fractionally. $\alpha_{\mathrm{res}}(T)$ is plotted in Fig. 8(b) as purple continuous curve.

The present resonator is very weakly constrained in its expansion, since it is supported on a midplane ring. Thus, the present measured CTF $\alpha_{\mathrm{res}}$ is very probably equal to the coefficient of thermal expansion (CTE) of silicon itself, $\alpha_{\mathrm{Si}}$, except for a minor correction due to the CTE of the coatings. This conclusion can be further substantiated by comparing the CTF of the resonator with the CTF of a horizontally oriented 25 cm long silicon resonator with a different, copper-and-steel support [32] (see Fig. 8(b), purple dashed curve). The very good agreement between the two measurements is a strong indication that both CTFs are equal to the CTE of silicon. To the best of authors' knowledge there are no other measured data of the silicon CTE in the studied temperature range. We also conclude that the support structure of the horizontal 25 cm resonator did not substantially constrain the thermal expansion of the resonator.

### 4.5. Resonator temperature instability

Fluctuations of resonator temperature, caused by small variations of cryostat cooling power over time, affect the length of the resonator even though the thermal expansion of the spacer material

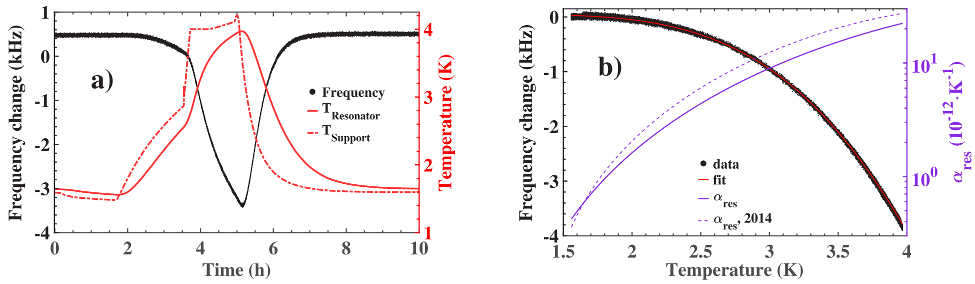


**Fig. 8.** Measurement of the thermal sensitivity coefficient in the temperature range between 1.58 K and 4.0 K. a) a heating-cooling cycle and the induced resonator frequency change. b) Relationship between resonator frequency change and temperature of resonator, and the computed CTF. The dashed purple line is a previous measurement on a different resonator [32].

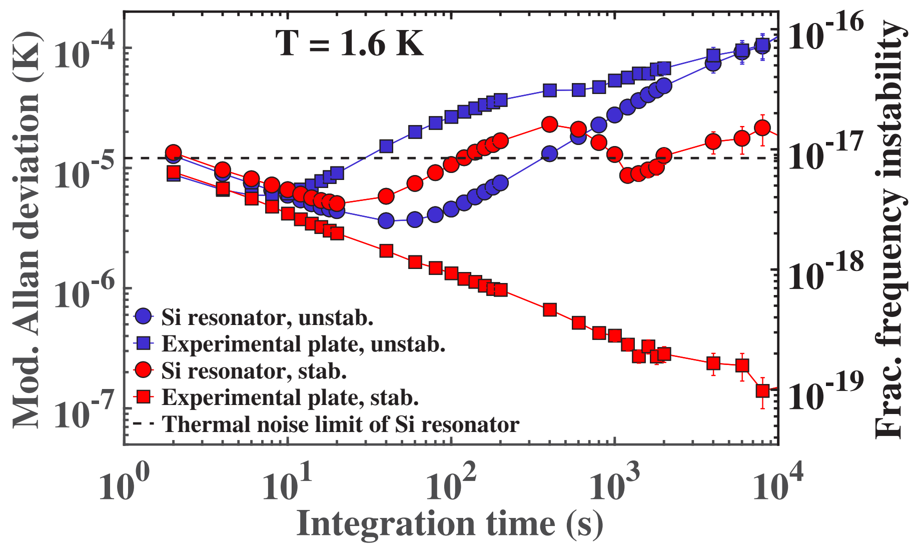


**Fig. 9.** Temperature instability of the experimentation plate and of the resonator with and without active temperature stabilization using data from the in-loop sensor at the experimental plate and the sensor attached directly to the middle ring of the resonator. Right ordinate axis is the calculated contribution to the resonator frequency instability arising from the temperature instability of the resonator.

is extremely small at the operating temperature. These fluctuations can be a limiting factor for the frequency stability of the resonator and thus must be characterized, and, if necessary, reduced by means of active temperature stabilization. Figure 9 shows in blue the temperature stability of the resonator and of the experimentation plate with no active stabilization of temperature. The temperature of the experimentation plate is measured with a sensor (Cernox) attached to the top surface near its center. Thanks to the poor thermal conductivity of the stainless-steel support structure the fluctuations of resonator temperature are reduced compared to those of the plate, for integration times $\tau$ between 10 s and 4000 s. Using the coefficient of thermal sensitivity $\alpha_{res}$ from the previous section, the resonator frequency instability due to the temperature fluctuations can be computed. It is indicated on the right ordinate axis of Fig. 9. We find that the frequency instability is below the thermal noise limit of the resonator, $8.5 \times 10^{-18}$ (dashed line in the figure), for integration times up to 400 s. But for longer integration times this is not the case any more: the frequency instability rises to $8 \times 10^{-17}$ at $\tau = 10^4$ s. While this level is not a concern in the present work, in order to allow reaching a thermal-noise-limited frequency stabilization in the future, an active stabilization of temperature is required. Therefore, we stabilized the temperature of the experimentation plate using a PID control acting on a heater attached at a distance of 15 mm from the sensor and on the top side of the experimentation plate. The result of the stabilization is also presented in Fig. 9 as red data. Now, the temperature-induced frequency instability is reduced and does not exceed $2 \times 10^{-17}$ for all integration times. For short, but not for all integration times, the instability is below the thermal noise limit. Hence, a further reduction of temperature instability by a factor of approximately 3 is desirable in the future. This should be achievable by optimization of the PID parameters.

## 5. Frequency stability of resonator

In the following sections we characterize the short-, medium-, and long-term stability of the resonator. The short-term stability was derived from the transmission photodiode signal. The medium-term and log-term stabilities were obtained with the frequency stabilization technique outlined in Sec. 3.3.

### *5.1. Short-term frequency stability*

To determine the short-term ($\tau$<1 s) stability of the silicon resonator relative to the stabilized ULE laser we use the data of the transmission photodiode signal when the laser frequency is tuned to the half-maximum of the resonance line (see Fig. 7(a)). The modified Allan deviation of the relative frequency variation is shown in Fig. 10(a). At 1 s integration time the instability is equal to 3 Hz ($2 \times 10^{-14}$). At integration times $\tau$<1 s the instability is higher and reaches a maximum of 40 Hz ($2.1 \times 10^{-13}$) at 90 ms integration time. This instability is a combination of contributions from the instability of the ULE laser, vibration-induced deformation of the silicon resonator, and the fiber-induced noises of the room-temperature and cryogenic fiber. The spectrum of the time trace from Fig. 7 is presented in Fig. 10(b). The vibration originating from the pulse-tube is weak for frequencies above 5 Hz, except for multiples of its 1.4 Hz base frequency. The broad peak at 13 Hz is typical for the seismic noise of our building. The strong peaks around 140 Hz are generated by the rotary valve of the pulse-tube and represent the dominant contribution to system instability at short-time scales.

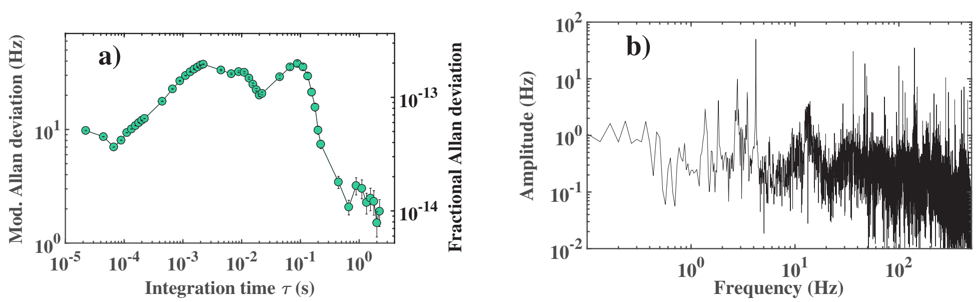


**Fig. 10.** Short-term frequency instability of the resonator. a) Modified Allan deviation and b) Spectrum of the time trace shown in Fig. 7.

### *5.2. Medium-term frequency instability*

The laser is stabilized to the cryogenic resonator using the fringe interrogation technique described above. The stabilized frequency is measured against a second maser with lower frequency

Optics EXPRESS

instability (designated as H-Maser 2 in Fig. 4). The result of a 10-h-long measurement is presented in Fig. 11. We determined a 210 $\mu$Hz/s frequency drift of the silicon resonator. This drift is removed before subsequent evaluation of the frequency instability. We also remove the ULE frequency drift from the recorded frequency shift $f_{\mathrm{AOM}}$ between the ULE laser and the silicon resonator (see Fig. 11(a), (bottom inset)).

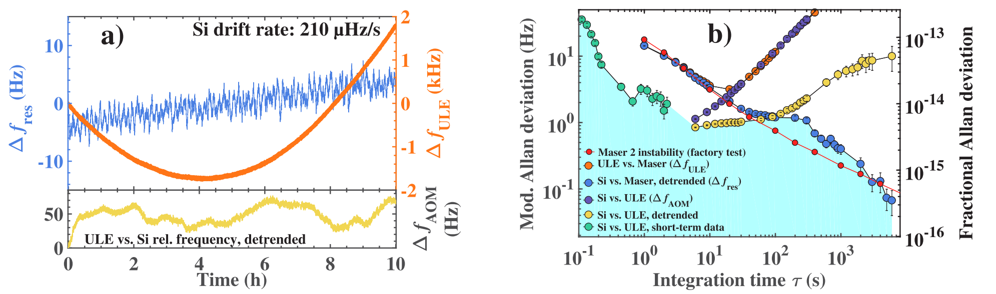


**Fig. 11.** a) A ten-hour-long frequency measurement of the silicon-resonator stabilized laser frequency (blue, running average over 100 s) and of the ULE-resonator-stabilized laser frequency (orange). The reference is an active hydrogen maser 2 with superior frequency stability. Bottom plot displays the difference between ULE resonator frequency and silicon resonator frequency, i.e. $\Delta f_{\mathrm{AOM}}$, where a second-order time variation of the ULE frequency was removed. b) Modified Allan deviation of various frequencies: short-term frequency stability of the silicon resonator imported from Fig. 10 (green), the stabilized laser frequency after removal of the 210 $\mu$Hz/s absolute frequency drift (blue), of the prestabilized ULE laser (orange), of the initial (blue violet) and corrected for ULE drift (light yellow) frequency difference between the ULE and silicon resonator. Red points represent the maser 2 instability specified by the manufacturer. The upper border of the light blue shaded area is the inferred instability of the silicon resonator.

The modified Allan deviation of the absolute laser (viz. silicon resonator) frequency is presented in Fig. 11(b). It follows closely the specified instability of the hydrogen maser, except for integration times $\tau$ between 200 s and 2000 s, where the laser instability is higher. We believe this increased level is due to the periodic oscillations of the resonator frequency (see Fig. 11(a)) caused by the variation of the temperature in the cryogenic laboratory and in the laboratory were the frequency comb is located. No in-depth search for parts of the equipment or optical setup sensitive to these temperature variations was done. This will be the subject of future work. The lowest instability of 0.067 Hz ($3.5 \times 10^{-16}$) was reached after 6000 s integration time. This value is limited by maser performance, according to its specifications.

The modified Allan deviation of the frequency shift $f_{\mathrm{AOM}}$ between ULE and silicon, corrected for ULE drift, is also plotted in yellow in the Fig. 11(b). For integration times between 10 s and 100 s this represents an upper bound for the frequency instability of the silicon resonator-stabilized laser. For integration times exceeding 100 s, a comparison with the H-maser rather than with the ULE resonator permits a more sensitive determination of the laser frequency noise, because on those time scales the ULE resonator drift is too strong. The employed line interrogation technique is slow (approximately 0.5 s cycle time). Therefore it is not effective in improving the frequency stability of a laser at short integration times. Moreover, on these time scales the acceleration induced fluctuations are important. The green discs in Fig. 11(b) (duplicated from Fig. 10(a)) show the expected instability of a laser locked to the silicon resonator if a more appropriate locking technique, such as the Pound-Drever-Hall technique, would be employed.

Optics EXPRESS

### 5.3. Long-term frequency drift

The long-term drift of the silicon resonator was measured relative to the H-maser (H-Maser 1 in Fig. 4) in the time interval between day 34 and day 266 after the completion of the cooldown (Fig. 12(a)). The measurements were done with the help of the prestabilized ULE laser using the line interrogation technique. Initially, the interrogation of the silicon resonator was performed once a day, for a duration of ~ 1 h and without active power stabilization. Later, starting on day 110 of the experiment, the laser was continuously stabilized to the resonator. During this period the power of the interrogating laser light was also stabilized. The temperature of the resonator was partially stabilized, as can be seen in Fig. 12(a). To account for the influence of temperature variations, frequency data are corrected using the value of $\alpha_{\mathrm{res}}(T)$. The maser frequency drift rate was determined as $3 \times 10^{-21}$/s and is removed from the silicon resonator frequency data.

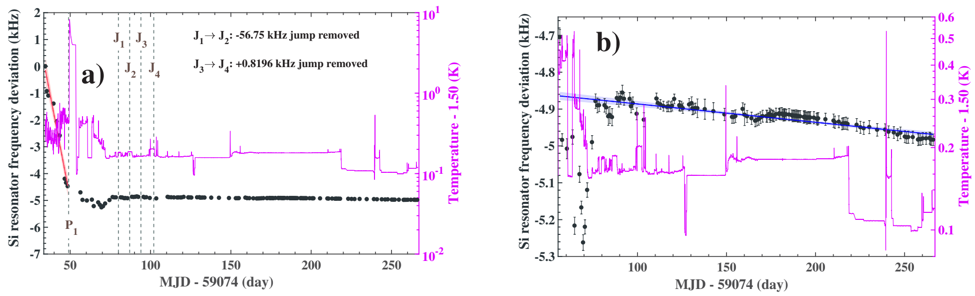


**Fig. 12.** a) Measurement of the long-term drift of the silicon resonator together with its temperature and b) zoom into the part of the measurement with the highest stability of the resonator.

The drift rate until day 49 was equal to $-3.6$ mHz/s or $-1.9 \times 10^{-17}$/s fractionally. After experiencing a short electricity blackout at the time marked $P_1$ in Fig. 12(a), the drift rate fell strongly. In the days following the blackout the temperature of the resonator increased to 10 K. We hypothesize that this small thermal cycle might have accelerated the relaxation of the silicon material.

During the time periods [$J_1$;$J_2$] and [$J_3$;$J_4$] we observed frequency jumps of $-56.75$ kHz and 0.82 kHz, respectively. The first frequency jump is possibly due to the erroneous read-out of another mode. The reason for the second jump was not found.

Stable frequency data was obtained starting with day 56. This data is presented in more detail in Fig. 11(b). Due to adjustment of the measurement procedures and laser light power the data has a larger spread at the beginning, until day ~ 80.

The mean frequency drift rate during the interval day 56 - 266 is equal to $-5.8$ $\mu$Hz/s or $-3.0 \times 10^{-20}$/s.

To reduce the scatter of the data, the transmitted laser power was stabilized to 3 $\mu$W and a continuous interrogation was implemented, starting on day 110. As can be seen in Fig. 13, this greatly improved the absolute frequency stability. Whereas the laser was always stabilized to the resonator, the measurements with the frequency comb were done with interruptions. This resulted in gaps in the data. According to the findings of Ref. [29] and later [33] the drift rate is highly dependent on the laser power used for interrogation. To study this effect, we reduced the optical power by a factor of 2 from 3 $\mu$W to 1.5 $\mu$W on day 168. As a result, the sign of the drift rate was opposite during the following 15 days. Subsequently, the drift rate became negative again.

Another interesting observation is a positive frequency offset of about 20 Hz after interruptions of the interrogation at day 120, 126, 158, and 246 (see Fig. 13). Contrary to this, a negative offset of approximately $-20$ Hz is observed at day 117 when the laser was not prestabilized to

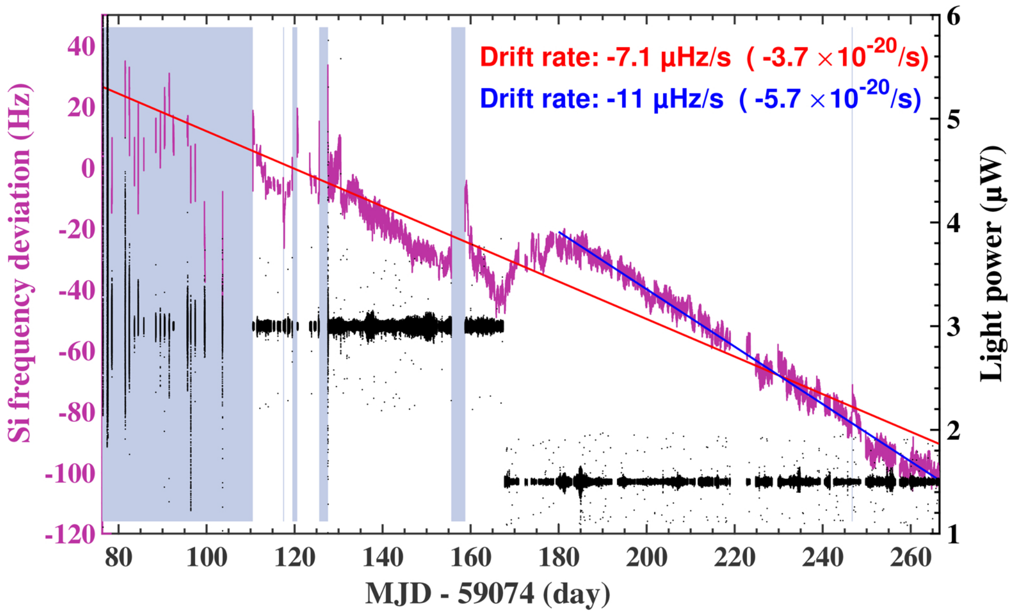


**Fig. 13.** Frequency change of the resonator (left y-axis) and the optical power impinging on the room-temperature end of the cryogenic fiber (right y-axis), during the most stable part of the measurement. During the light blue shaded intervals the resonator was interrogated with interruptions. The silicon resonator frequency data was averaged over 600 s.

the ULE resonator, the laser light was impinging on the bottom mirror of the resonator, and the light power was increased to maximum by the power stabilization electronics, that did not detect any transmitted light. The observed frequency offsets occur perhaps because of some relaxation process in the mirror coatings.

The mean drift rate over the whole 190-day-long time interval after day 76 was $-7.13$ $\mu$Hz/s or $-3.7 \times 10^{-20}$/s (see Fig. 13). The mean drift rate for the stable interval after adjustment of the laser power was slightly higher, $-10.9$ $\mu$Hz/s or $-5.7 \times 10^{-20}$/s.

## 6. Conclusion

We developed an apparatus that permits to stabilize a laser to a cryogenic optical resonator with good performance in terms of frequency stability on medium time scale and excellent long-term stability.

A 190 mm long silicon optical resonator was developed for this purpose. It is vertically oriented, and its design was optimized for low vibration sensitivity. The temperature instability of the resonator was determined not to be a current limiting factor to the frequency stability. We measured the coefficient of thermal sensitivity of the resonator frequency to be close to $1 \times 10^{-12}\mathrm{K}^{-1}$, a value that is expected to be essentially the thermal expansion coefficient of the silicon crystal itself. The resonator's sensitivity to vibrations was determined using the vibrations produced by the cryostat. We found the sensitivity to be approximately $4 \times 10^{-10}/g$ in fractional terms. This relatively high value could potentially be be lowered by a careful alignment of the resonator to the support points.

An overall display of the frequency instability of the system is provided by the light blue filling in Fig. 11(b). The stability is $2 \times 10^{-14}$ at one second integration time, but since the laser was not actually stabilized effectively to the resonator on this time scale, this number reflects the stability of the resonator system only. The medium-term stability of the stabilized laser is approximately

$4.8 \times 10^{-15}$ at 10 s integration time. This is an upper limit, as the instability of the reference of this measurement, the ULE resonator, is not negligible. The instability remains at this level up to 100 s integration time and then decreases to $3.5 \times 10^{-16}$ at 6000 s integration time. This value is limited by the performance of the maser that was available for the characterization.

The long-term performance of the system is excellent. It is notable that the apparatus was functional for almost one year at the temperature below 1.7 K. The long-term drift of the resonator was followed over 266 days. During a 190-day-long period the frequency change was 117 Hz or $6.1 \times 10^{-13}$ in fractional terms. This corresponds to a drift rate of $-7.1\ \mu$Hz/s or $-3.7 \times 10^{-20}$/s. This result was achieved with the laser continuously interrogating the silicon resonator. The drift rate is approximately ten times higher than the drift rate of the active hydrogen maser used for comparison ($3 \times 10^{-21}$/s). It is also higher than the drift rates of the two most stable silicon resonators demonstrated so far, one at 1.5 K [18] and one at 124 K [40], having drift rates of $5.9 \pm 3.8 \times 10^{-21}$/s measured over 163 days and of $9 \times 10^{-21}$/s measured over 45 days, respectively.

With this long-term performance, the optical reference can provide - without requiring a H-maser - optical frequencies with attractive absolute frequency uncertainties, as follows. The optically stabilized frequency comb delivers a high-purity RF signal at 250 MHz. This could be converted into a nominally 10 MHz signal to be used as reference for the GNSS receiver. Via common-view GNSS with a metrology institute, the 10 MHz signal frequency can be measured relative to an atomic frequency (as was done here). The measurement yields a correction that can be taken into account in data processing, or that can be sent to an acousto-optic frequency shifter that shifts the optical frequency. We estimate that the absolute uncertainty of the average optical frequency will then be in the low $10^{-14}$ range. This estimate follows from a combination of contributions: (i) the common-view comparison has an intrinsic instability of approximately $1 \times 10^{-14}$ for an integration time of $10^5$ s, in our laboratory; (ii) the instability of the cryogenic reference is probably at this level (it has not been measured for this integration time value, but see Fig. 11(b)); (iii) the drift over the same interval is of order $1 \times 10^{-14}$ (blue line in Fig. 13). Thus, the day-averaged optical frequency can be determined with uncertainty in the low $10^{-14}$ range.

While within this study, the frequency comb was locked to the prestabilized laser, it would alternatively be possible to lock it to a laser directly locked to the cryogenic cavity, thus simplifying the setup.

We identified a number of issues that limit the stability at short and medium integration times: residual vibrations, cryogenic fiber noise due to vibrations of the cryostat and the influence of lab temperature. Future mitigation of these issues is expected to improve the overall performance of this system, eventually allowing to reach the thermal-noise-limited performance of the resonator.

**Funding.** Deutsche Forschungsgemeinschaft (INST 208/548-1 FUGG, INST 208/774-1 FUGG, SCHI 431/21-1); Ministerium für Kultur und Wissenschaft des Landes Nordrhein-Westfalen (INST 208/548-1 FUGG, INST 208/774-1 FUGG).

**Acknowledgment.** We thank M. G. Hansen for his help with the operation of the frequency comb and U. Rosowski for the preparation of the GNSS comparison data.

**Disclosures.** The authors declare no conflicts of interest.

**Data Availability.** Data underlying the results presented in this paper are not publicly available at this time but may be obtained from the authors upon reasonable request.

## References

1. A. D. Ludlow, M. M. Boyd, J. Ye, E. Peik, and P. O. Schmidt, "Optical atomic clocks," Rev. Mod. Phys. **87**(2), 637–701 (2015).
2. L. Ju, D. G. Blair, and C. Zhao, "Detection of gravitational waves," Rep. Prog. Phys. **63**(9), 1317–1427 (2000).
3. C. M. Will, "The confrontation between general relativity and experiment," Living Rev. Relativ. **17**(1), 4 (2014).
4. R. X. Adhikari, "Gravitational radiation detection with laser interferometry," Rev. Mod. Phys. **86**(1), 121–151 (2014).
5. N. Poli, C. W. Oates, P. Gill, and G. M. Tino, "Optical atomic clocks," Rivista del Nuovo Cimento **36**, 555 (2013).
6. Y. V. Stadnik and V. V. Flambaum, "Enhanced effects of variation of the fundamental constants in laser interferometers and application to dark-matter detection," Phys. Rev. A **93**(6), 063630 (2016).

Optics EXPRESS


7. A. A. Geraci, C. Bradley, D. Gao, J. Weinstein, and A. Derevianko, "Searching for Ultralight Dark Matter with Optical Cavities," Phys. Rev. Lett. **123**(3), 031304 (2019).
8. C. J. Kennedy, E. Oelker, J. M. Robinson, T. Bothwell, D. Kedar, W. R. Milner, G. E. Marti, A. Derevianko, and J. Ye, "Precision Metrology Meets Cosmology: Improved Constraints on Ultralight Dark Matter from Atom-Cavity Frequency Comparisons," Phys. Rev. Lett. **125**(20), 201302 (2020).
9. R. Oswald, A. Nevsky, V. Vogt, S. Schiller, N. Figueroa, K. Zhang, O. Tretiak, D. Antypas, D. Budker, A. Banerjee, and G. Perez, "Search for dark-matter-induced oscillations of fundamental constants using molecular spectroscopy," Phys. Rev. Lett. **129**(3), 031302 (2022).
10. S. Doeleman, T. Mai, A. E. E. Rogers, J. G. Hartnett, M. E. Tobar, and N. Nand, "Adapting a Cryogenic Sapphire Oscillator for Very Long Baseline Interferometry," Publ. Astron. Soc. Pac. **123**(903), 582–595 (2011).
11. C.-H. Li, A. J. Benedick, P. Fendel, A. G. Glenday, F. X. Kärtner, D. F. Phillips, D. Sasselov, A. Szentgyorgyi, and R. L. Walsworth, "A laser frequency comb that enables radial velocity measurements with a precision of 1 cm $s^{-1}$," Nature **452**(7187), 610–612 (2008).
12. T. Herr and R. A. McCracken, "Astrocombs: Recent Advances," IEEE Photonics Technol. Lett. **31**(23), 1890–1893 (2019).
13. J. Grotti, S. Koller, S. Vogt, *et al.*, "Geodesy and metrology with a transportable optical clock," Nat. Phys. **14**(5), 437–441 (2018).
14. C. Lisdat, G. Grosche, N. Quintin, *et al.*, "A clock network for geodesy and fundamental science," Nat. Commun. **7**(1), 12443 (2016).
15. T. Takano, M. Takamoto, I. Ushijima, N. Ohmae, T. Akatsuka, A. Yamaguchi, Y. Kuroishi, H. Munekane, B. Miyahara, and H. Katori, "Geopotential measurements with synchronously linked optical lattice clocks," Nat. Photonics **10**(10), 662–666 (2016).
16. M. Nagel, S. R. Parker, E. V. Kovalchuk, P. L. Stanwix, J. G. Hartnett, E. N. Ivanov, A. Peters, and M. E. Tobar, "Direct terrestrial test of Lorentz symmetry in electrodynamics to $10^{-18}$," Nat. Commun. **6**(1), 8174–8176 (2015).
17. Q. Chen, E. Magoulakis, and S. Schiller, "High-sensitivity crossed-resonator laser apparatus for improved tests of Lorentz invariance and of space-time fluctuations," Phys. Rev. D **93**(2), 022003 (2016).
18. E. Wiens, A. Y. Nevsky, and S. Schiller, "Resonator with ultrahigh length stability as a probe for equivalence-principle-violating physics," Phys. Rev. Lett. **117**(27), 271102 (2016).
19. P. Delva, J. Lodewyck, S. Bilicki, *et al.*, "Test of special relativity using a fiber network of optical clocks," Phys. Rev. Lett. **118**(22), 221102 (2017).
20. A. Takahashi, "Long-term dimensional stability of a line scale made of low thermal expansion ceramic NEXCERA," Meas. Sci. Technol. **23**(3), 035001 (2012).
21. K. Hosaka, H. Inaba, D. Akamatsu, M. Yasuda, J. Sugawara, A. Onae, and F.-L. Hong, "A Fabry-Perot etalon with an ultralow expansion ceramic," Jpn. J. Appl. Phys. **52**(3R), 032402 (2013).
22. I. Ito, A. Silva, T. Nakamura, and Y. Kobayashi, "Stable cw laser based on low thermal expansion ceramic cavity with 4.9 mHz/s frequency drift," Opt. Express **25**(21), 26020 (2017).
23. C. J. Kwong, M. G. Hansen, J. Sugawara, and S. Schiller, "Characterization of the long-term dimensional stability of a NEXCERA block using the optical resonator technique," Meas. Sci. Technol. **29**(7), 075011 (2018).
24. K. Numata, A. Kemery, and J. Camp, "Thermal-noise limit in the frequency stabilization of lasers with rigid cavities," Phys. Rev. Lett. **93**(25), 250602 (2004).
25. S. Seel, R. Storz, G. Ruoso, J. Mlynek, and S. Schiller, "Cryogenic Optical Resonators: A new tool for laser frequency stabilization at the 1 Hz level," Phys. Rev. Lett. **78**(25), 4741–4744 (1997).
26. R. Storz, C. Braxmaier, K. Jäck, O. Pradl, and S. Schiller, "Ultrahigh long-term dimensional stability of a sapphire cryogenic optical resonator," Opt. Lett. **23**(13), 1031 (1998).
27. D. G. Matei, T. Legero, S. Häfner, C. Grebing, R. Weyrich, W. Zhang, L. Sonderhouse, J. M. Robinson, J. Ye, F. Riehle, and U. Sterr, "1.5 $\mu$m lasers with sub-10 mHz linewidth," Phys. Rev. Lett. **118**(26), 263202 (2017).
28. W. Zhang, J. M. Robinson, L. Sonderhouse, E. Oelker, C. Benko, J. L. Hall, T. Legero, D. G. Matei, F. Riehle, U. Sterr, and J. Ye, "Ultrastable silicon cavity in a continuously operating closed-cycle cryostat at 4 K," Phys. Rev. Lett. **119**(24), 243601 (2017).
29. J. M. Robinson, E. Oelker, W. R. Milner, W. Zhang, T. Legero, D. G. Matei, F. Riehle, U. Sterr, and J. Ye, "Crystalline optical cavity at 4 K with thermal-noise-limited instability and ultralow drift," Optica **6**(2), 240 (2019).
30. T. Kessler, C. Hagemann, C. Grebing, T. Legero, U. Sterr, F. Riehle, M. J. Martin, L. Chen, and J. Ye, "A sub-40-mHz-linewidth laser based on a silicon single-crystal optical cavity," Nat. Photonics **6**(10), 687–692 (2012).
31. C. Hagemann, C. Grebing, C. Lisdat, S. Falke, T. Legero, U. Sterr, F. Riehle, M. Martin, and J. Ye, "Ultra-stable laser with average fractional frequency drift rate below $5\times10^{-19}$/s," Opt. Lett. **39**(17), 5102 (2014).
32. E. Wiens, Q. Chen, I. Ernsting, H. Luckmann, A. Y. Nevsky, U. Rosowski, and S. Schiller, "A silicon single-crystal cryogenic optical resonator," Opt. Lett. **39**(11), 3242 (2014).
33. E. Wiens, C. J. Kwong, T. Müller, and S. Schiller, "A simplified cryogenic optical resonator apparatus providing ultra-low frequency drift," Rev. Sci. Instrum. **91**(4), 045112 (2020).
34. E. Wiens and S. Schiller, "A simple and efficient passive vibration isolation system for large loads in closed-cycle cryostats," Rev. Sci. Instrum. **92**(9), 095101 (2021).
35. J. J. Hall, "Electronic Effects in the Elastic Constants of n-Type Silicon," Phys. Rev. **161**(3), 756–761 (1967).
36. Ansys® Academic Research Mechanical, Release 2020 R1.

Optics EXPRESS


37. S. M. Sze and M.-K. Lee, *Semiconductor Devices: Physics and Technology* (Wiley, 2012).
38. T4Science iMaser 3000/BAT1/HCB/LN/MS/O2/RE/W3, serial number: iMaser 147.
39. L.-S. Ma, P. Jungner, J. Ye, and J. L. Hall, "Delivering the same optical frequency at two places: accurate cancellation of phase noise introduced by an optical fiber or other time-varying path," Opt. Lett. **19**(21), 1777 (1994).
40. C. Hagemann, "Ultra-stable laser based on a cryogenic single-crystal silicon cavity," Ph.D. thesis, Gottfried Wilhelm Leibniz Universität Hannover, Hannover, Germany (2013).